Spectroscopy of _{Λ}^{9}Li by electroproduction

G. M. Urciuoli *et al.* (Jefferson Lab Hall A Collaboration)

Phys. Rev. C **91**, 034308 — Published 4 March 2015

DOI: 10.1103/PhysRevC.91.034308

Spectroscopy of ${}^{9}_{\Lambda}$Li by electroproduction

G.M. Urciuoli,[1] F. Cusanno,[1,*] S. Marrone,[2] A. Acha,[3] P. Ambrozewicz,[3] K.A. Aniol,[4] P. Baturin,[3] P.Y. Bertin,[5] H. Benaoum,[6] K.I. Blomqvist,[7] W.U. Boeglin,[3] H. Breuer,[8] P. Brindza,[9] P. Bydžovský,[10] A. Camsonne,[5] C.C. Chang,[8] J.-P. Chen,[9] Seonho Choi,[11] E.A. Chudakov,[9] E. Cisbani,[12] S. Colilli,[12] L. Coman,[3] B.J. Craver,[13] G. De Cataldo,[2] C.W. de Jager,[9,13] R. De Leo,[2] A.P. Deur,[13] C. Ferdi,[5] R.J. Feuerbach,[9] E. Folts,[9] R. Fratoni,[12] S. Frullani,[12] F. Garibaldi,[12] O. Gayou,[14] F. Giuliani,[12] J. Gomez,[9] M. Gricia,[12] J.O. Hansen,[9] D. Hayes,[15] D.W. Higinbotham,[9] T.K. Holmstrom,[16] C.E. Hyde,[15,5] H.F. Ibrahim,[15,17] M. Iodice,[18] X. Jiang,[19] L.J. Kaufman,[20] K. Kino,[21] B. Kross,[9] L. Lagamba,[2] J.J. LeRose,[9] R.A. Lindgren,[13] M. Lucentini,[12] D.J. Margaziotis,[4] P. Markowitz,[3] Z.E. Meziani,[11] K. McCormick,[19] R.W. Michaels,[9] D.J. Millener,[22] T. Miyoshi,[23] B. Moffit,[16] P.A. Monaghan,[14] M. Moteabbed,[3] C. Muñoz Camacho,[24] S. Nanda,[9] E. Nappi,[2] V.V. Nelyubin,[13] B.E. Norum,[13] Y. Okasyasu,[23] K.D. Paschke,[20] C.F. Perdrisat,[16] E. Piasetzky,[25] V.A. Punjabi,[26] Y. Qiang,[14] P.E. Reimer,[27] J. Reinhold,[3] B. Reitz,[9] R.E. Roche,[28] V.M. Rodriguez,[29] A. Saha,[9,*] F. Santavenere,[12] A.J. Sarty,[30] J. Segal,[9] A. Shahinyan,[31] J. Singh,[13] S. Širca,[32] R. Snyder,[13] P.H. Solvignon,[11] M. Sotona,[10,*] R. Subedi,[33] V.A. Sulkosky,[16] T. Suzuki,[23] H. Ueno,[34] P.E. Ulmer,[15] P. Veneroni,[12] E. Voutier,[35] B.B. Wojtsekhowski,[9] X. Zheng,[27,13] and C. Zorn[9]

(Jefferson Lab Hall A Collaboration)

[1] *Istituto Nazionale di Fisica Nucleare, Sezione di Roma, Piazzale A. Moro 2, I-00185 Rome, Italy*
[2] *Istituto Nazionale di Fisica Nucleare, Sezione di Bari and University of Bari, I-70126 Bari, Italy*
[3] *Florida International University, Miami, Florida 33199, USA*
[4] *California State University, Los Angeles, Los Angeles California 90032, USA*
[5] *Université Blaise Pascal/IN2P3, F-63177 Aubière, France*
[6] *Department of Applied Physics, University of Sharjah, UAE*
[7] *Universität Mainz, Mainz, Germany*
[8] *University of Maryland, College Park, Maryland 20742, USA*
[9] *Thomas Jefferson National Accelerator Facility, Newport News, Virginia 23606, USA*
[10] *Nuclear Physics Institute, Řež near Prague, Czech Republic*
[11] *Temple University, Philadelphia, Pennsylvania 19122, USA*
[12] *Istituto Nazionale di Fisica Nucleare, Sezione di Roma, gruppo collegato Sanità, and Istituto Superiore di Sanità, I-00161 Rome, Italy*
[13] *University of Virginia, Charlottesville, Virginia 22904, USA*
[14] *Massachussets Institute of Technology, Cambridge, Massachusetts 02139, USA*
[15] *Old Dominion University, Norfolk, Virginia 23508, USA*
[16] *College of William and Mary, Williamsburg, Virginia 23187, USA*
[17] *Physics Department, Cairo University, Giza 12613, Egypt*
[18] *Istituto Nazionale di Fisica Nucleare, Sezione di Roma Tre, I-00146 Rome, Italy*
[19] *Rutgers, The State University of New Jersey, Piscataway, New Jersey 08855, USA*
[20] *University of Massachussets Amherst, Amherst, Massachusetts 01003, USA*
[21] *Research Center for Nuclear Physics, Osaka University, Ibaraki, Osaka 567-0047, Japan*
[22] *Brookhaven National Laboratory, Upton, New York 11973, USA*
[23] *Tohoku University, Sendai, 980-8578, Japan*
[24] *CEA Saclay, DAPNIA/SPhN, F-91191 Gif-sur-Yvette, France*
[25] *School of Physics and Astronomy, Sackler Faculty of Exact Science, Tel Aviv University, Tel Aviv 69978, Israel*
[26] *Norfolk State University, Norfolk, Virginia 23504, USA*
[27] *Physics Division, Argonne National Laboratory, Argonne, Illinois 60439, USA*
[28] *Florida State University, Tallahassee, Florida 32306, USA*
[29] *University of Houston, Houston, Texas 77204, USA*
[30] *St. Mary's University, Halifax, Nova Scotia, Canada*
[31] *Yerevan Physics Institute, Yerevan, Armenia*
[32] *Dept. of Physics, University of Ljubljana, Slovenia*
[33] *Kent State University, Kent, Ohio 44242, USA*
[34] *Yamagata University, Yamagata 990-8560, Japan*
[35] *LPSC, Université Joseph Fourier, CNRS/IN2P3, INPG, F-38026 Grenoble, France*

(Dated: January 22, 2015)

Background: In the absence of accurate data on the free two-body hyperon-nucleon interaction, the spectra of hypernuclei provides information on the details of the effective hyperon-nucleon interaction.

Purpose: To obtain a high-resolution binding energy spectrum for the ${}^{9}\mathrm{Be}(e,e'K^{+})^{9}_{\Lambda}\mathrm{Li}$ reaction.

Method: Electroproduction of the hypernucleus ${}^{9}_{\Lambda}$Li has been studied for the first time with sub-MeV energy resolution in Hall A at Jefferson Lab on a ^{9}Be target. In order to increase the counting rate and to provide unambiguous kaon identification, two superconducting septum magnets and a Ring Imaging CHerenkov detector (RICH) were added to the Hall A standard equipment.

Results: The cross section to low-lying states of ${}^{9}_{\Lambda}$Li is concentrated within 3 MeV of the ground state and can be fitted with four peaks. The positions of the doublets agree with theory while a disagreement could exist with respect to the relative strengths of the peaks in the doublets. The Λ separation energy, B_Λ, of 8.36 $\pm$ 0.08 (stat.) $\pm$ 0.08 (syst.) MeV was measured, in agreement with an earlier experiment.

PACS numbers: 21.80.+a, 25.30.Rw, 21.60.Cs, 24.50.+g

I. INTRODUCTION

Hypernuclei provide a unique laboratory for the investigation of hadronic many-body systems with strangeness -1 and for the study of new aspects of the strong and weak interactions in nuclei. Because direct measurements of hyperon-nucleon (YN) scattering at low energies are prohibited by the short hyperon lifetime, hypernuclear spectra are the only way to study this interaction. Thus, a unique opportunity to obtain this information is provided by observing the fine structure of hypernuclei caused by the specific spin-dependence of the hyperon-nucleon interaction. Such characteristics are realized in practice only in Λ hypernuclei and are hardly seen in other hypernuclei. Thus the spectroscopy of Λ hypernuclei has a unique value in strangeness nuclear physics.

In the past, hypernuclear spectroscopy has been carried out with limited resolution only by means of hadronic reactions, such as the strangeness exchange and associated production reactions, that use meson beams and in which a neutron is converted into a Λ [1]. More recently, γ-ray spectroscopy has been used to measure hypernuclear transition energies. Here, a few-keV energy resolution has been obtained, which has allowed precise level assignments and the measurement of doublet spacings [2]. However, the method is limited to the bound region below particle emission thresholds and to bound levels reached following particle emission.

The experimental knowledge can be enhanced using the $(e,e'K^+)$ electroproduction reaction. This reaction is characterized by a large momentum transfer to the hypernucleus ($q \gtrsim 250$ MeV/c) and strong spin-flip contributions, even at zero K^+ production angles [3], resulting in the excitation of both natural- and unnatural-parity states [4, 5]. In the $(e,e'K^+)$ reaction a proton is converted into a Λ hyperon so that one can produce and study new hypernuclei, not accessible in the standard reactions.

Together with experiments in Hall C [6–8], the E94-107 experiment in Hall A at Jefferson Lab [9] started a systematic study of high resolution hypernuclear spectroscopy in the 0p-shell region of nuclei, such as the hypernuclei produced in electroproduction on ^{9}Be, ^{12}C, and ^{16}O targets. Results on ${}^{12}_{\Lambda}$B and ${}^{16}_{\Lambda}$N have been published [4, 5]. The results for ${}^{9}_{\Lambda}$Li, which was long ago suggested as a good candidate for electroproduction studies [10] because of the predicted large splitting of the ground-state and second-excited-state doublets are presented in this paper.

II. THEORY

As in the previous experiments [4, 5], the data are interpreted using shell-model calculations that include both Λ and Σ hyperons in 0s states coupled to p-shell core wave functions optimized to fit a wide range of p-shell properties [11, 12]. The $(e,e'K^+)$ reaction is described with distorted-wave impulse approximation (DWIA) calculations [10] that use the Saclay-Lyon (SLA) model [13] for the elementary $p(e,e'K^+)\Lambda$ reaction. The SLA model was successfully applied in the analysis of electroproduction experiments on ^{12}C and ^{16}O targets [4, 5], which suggests that this model provides a reasonable prediction for the elementary cross section at very small K^+ production angles and at the center of mass energy of this experiment.

In a shell-model approach, one can define five $p_N s_\Lambda$ two-body matrix elements for a hypernucleus with an s-level Λ coupled to a p-shell nuclear core. These can be put into a one-to-one correspondence with the parameters (radial integrals) $\overline{V}$, Δ, S_Λ, S_N, and T associated with the average central, spin-spin, Λ-spin-orbit, nucleon-spin-orbit, and tensor components of the in-medium (effective) ΛN interaction [14], given by

$$V_{\Lambda N} = \overline{V} + \Delta \mathbf{s}_N \cdot \mathbf{s}_\Lambda + S_\Lambda \mathbf{l}_N \cdot \mathbf{s}_\Lambda + S_N \mathbf{l}_N \cdot \mathbf{s}_N + T S_{12}, \quad (1)$$

where $\mathbf{s}$ denotes the spin and $\mathbf{l}$ the angular momentum. The constant $\overline{V}$ simply contributes $n\overline{V}$ to the binding energy of every $p^n s_\Lambda$ configuration and therefore does not affect the spectrum, only the overall binding energy B_Λ. The value of $\overline{V} = -1.23$ MeV used is very close to the value that reproduces the experimental B_Λ value (Table 2 of Ref. [12]). In the weak-coupling limit (quite good because the ΛN interaction for s_Λ is a spatial monopole), only operators that depend on the spin of the Λ particle (Δ, S_Λ, T) contribute to doublet spacings while S_N contributes to the spacing between doublets. We use values (in MeV)

$$\Delta = 0.43 \quad S_\Lambda = -0.015 \quad S_N = -0.39 \quad T = 0.03\,, \quad (2)$$

* Deceased

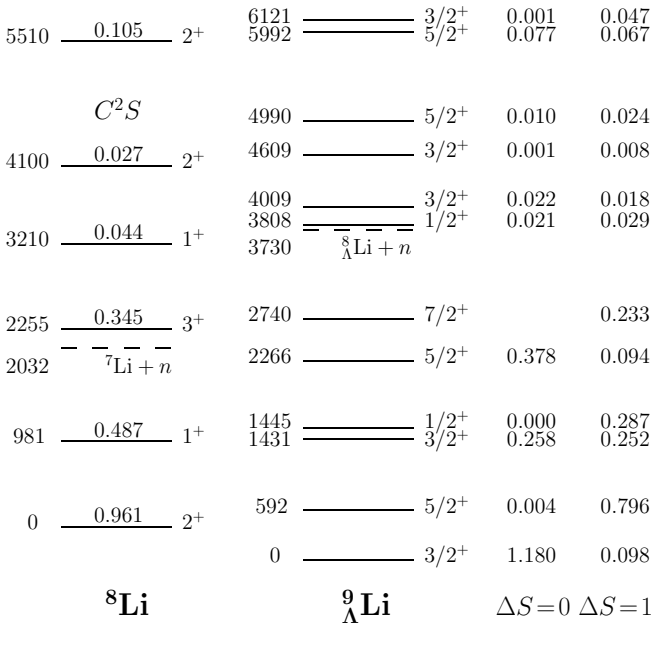

FIG. 1. The calculated spectrum of $^9_\Lambda$Li. The ^{8}Li core states are shown on the left along with the spectroscopic factors for proton removal from ^{9}Be. All excitation energies are in keV. On the right, the factors giving the relative population of levels in purely non-spin-flip ($\Delta S=0$) and purely spin-flip ($\Delta S=1$) production reactions on ^{9}Be are given.

that fit the spectrum of the five bound levels of $^7_\Lambda$Li determined from $(\pi^+, K^+\gamma)$ and $(K^-, \pi^-\gamma)$ experiments. The main parameters used for the corresponding ΛN-ΣN interaction are $\overline{V}'=1.45$ and $\Delta'=3.04$ MeV, making a total of six YN parameters that affect the spectrum.

The calculated spectrum for $^9_\Lambda$Li is shown in Fig. 1, together with the core states for ^{8}Li (the first four are known and the other two are taken from the p-shell calculation), while Table I shows the contributions to the various level spacings for the three lowest doublets. The contributions listed in Table I do not add up to exactly the spacings in Fig. 1 because small contributions from configuration mixing are not included (see the caption to Table I). The spectroscopic factors (C^2S with $C^2=2/3$) for proton removal from ^{9}Be control the population of $^9_\Lambda$Li states via electroproduction. The structure factors on the right of the figure for pure non-spin-flip and spin-flip transitions [12] are normalized such that in the weak-coupling limit (YN interactions turned off) the $\Delta S=0$ and $\Delta S=1$ values for a doublet each sum to C^2S for the core state.

The C^2S values for $^9\mathrm{Be}\rightarrow{}^8$Li in Fig.1 are in good agreement with the values from $(d,^3\mathrm{He})$ studies [15, 16] (see Table II). From a (t,α) study [18], larger relative values were extracted for the excited 1^+ and 3^+ states of ^{8}Li. The C^2S values for the interaction used in the present work are listed in Fig. 1. The values for all the p-shell interactions derived in connection with these hypernuclear studies are similar and in agreement with those for the Cohen and Kurath (6-16)2BME interaction [19]. The values for the other two Cohen and Kurath interactions put more strength in the second 1^+ state than in the first (as noted in Ref. [19] for the (8-16)POT interaction). The reason for this is that the 1^+_1 states are rather purely $L=1$, $S=1$, rather than with strongly mixed $S=0$ and $S=1$ components, as happens for the other interactions. Strength for the 1^+_2 state would be immediately noticeable in electroproduction because the $^9_\Lambda$Li states based on the 1^+_2 state lie close to the neutron threshold at 3.73 MeV and should therefore be narrow.

The states in the first-excited doublet are predicted to be nearly degenerate, in part because of the contribu-

TABLE I. Contributions to energy-level spacings (in keV) from the components of the ΛN interaction. The coefficients of the parameters are determined by numerical differentiation. The contribution from Λ-Σ coupling is determined by diagonalizing with the coupling switched on and off. The difference between the total contribution of 601 keV in the first line of the table and the 592 keV from diagonalization (see Fig. 1) is due to small differences in the sum of diagonal core energies caused by configuration mixing. Such differences are usually only a few tens of keV.

$J^\pi_i-J^\pi_f$	$\Lambda\Sigma$	Δ	S_Λ	S_N	T
$\frac{5}{2}^+_1-\frac{3}{2}^+_1$	116	531	−18	−18	−10
$\frac{1}{2}^+_1-\frac{3}{2}^+_2$	79	−229	13	11	91
$\frac{7}{2}^+_1-\frac{5}{2}^+_2$	90	494	−34	−15	−51
$\frac{3}{2}^+_2-\frac{3}{2}^+_1$	63	441	−12	56	−42
$\frac{7}{2}^+_1-\frac{5}{2}^+_1$	-6	8	−7	−77	−22

TABLE II. The C^2S values for proton removal from ^{9}Be. The second through fourth columns contain the normalized experimental values, for the $(d,^3\mathrm{He})$ reactions (second and third columns) and normalized to the same summed strength (number of p-shell protons in ^{9}Be) for the (t,α) reaction (fourth column). The values for one of the other interactions used in hypernuclear calculations are listed in the fifth column and the values from the Cohen and Kurath (6-16)2BME and the (8-16)2BME interactions [17] in the sixth and seventh columns.

J^π_i	[15]	[16]	[18]	fit4	(6-16)	(8-16)
2^+_1	1.00	1.03	0.78	1.00	1.00	0.95
1^+_1	0.42	0.39	0.47	0.45	0.40	0.20
3^+_1	0.33	0.30	0.51	0.36	0.35	0.33
1^+_2				0.04	0.06	0.24

tions from Λ-Σ coupling (see Table I). In addition, the $3/2_2^+$ state contains a 3.5% admixture of a Λ coupled to the ^{8}Li ground state which lowers the $3/2_2^+$ state by another ≈ 35 keV. Thus, if the shell-model predictions are reasonable, five peaks should, in principle, be resolved in $^9_\Lambda$Li below the particle-decay threshold by an electroproduction experiment with good energy resolution.

III. EXPERIMENT

Hall A at JLab is well suited to perform $(e, e'K^+)$ experiments. Scattered electrons are detected in the High Resolution Spectrometer (HRS) electron arm while coincident kaons are detected in the HRS hadron arm [20]. The disadvantage of smaller electromagnetic cross sections is compensated for by the high current and high duty cycle properties of the beam. Throughout the experiment, the same equipment has been used in very similar kinematical conditions on C, Be, and H_2O targets. The use of a pair of septum magnets permitted particle detection at very forward angles [21] and a Ring Imaging CHerenkov (RICH) detector [22–25] has been used in the hadron arm to provide an unambiguous identification of kaons when combined with the standard particle identification apparatus of Hall A, based on aerogel Cherenkov detectors [26–28]. In the present experiment a 92.5 mg/cm^2 solid ^{9}Be target with a beam current of ∼100 μA was used at a beam energy of 3775 MeV. Both HRSs were physically positioned at an angle of 12.5°, but the pair of septum magnets yielded an effective angle for both the scattered electron and the hadron detection of ∼ 6°.

Fig. 2 shows the observed binding-energy spectrum of $^9_\Lambda$Li. The broad peak centered at a small positive binding energy corresponds to the $^9_\Lambda$Li states in Fig. 1 corresponding to the lowest three states of ^{8}Li. The rise in cross section starting at 0 MeV corresponds to states with the Λ in a p orbit and, because these states are unbound, the states are broad and no structure is observed. As in Ref. [4, 5], the background was determined from the binding energy spectrum obtained with a coincidence time shifted with respect to the coincidence time between secondary electrons and produced kaons and was rather flat for values of binding energy ranging from 15 MeV to 0 MeV. Its value was calculated as the average of the counts in the range 9.95 MeV ≤ Binding energy ≤ 18.35 MeV.

For the calculation of the absolute cross section, we computed the following quantities: detector efficiencies, detector dead time, detector phase space, kaon survival in HRS, integrated luminosity. The calculations of efficiencies for the standard HRS package are well established and implemented in the Hall A analysis software. Therefore, those procedures were used for that purpose. For the RICH and aerogel Cherenkov detectors, we used one detector to determine the efficiency of the other one in the following way: we selected a pure sample of kaons by means of aerogel detectors and we measured the fraction of those kaons detected by the RICH and vice versa. The detector dead time was measured by the Hall A data acquisition system. The detector phase space was calculated using the SIMC code [29]. Kaon survival is calculated considering the average path length inside the HRS arm. The integrated luminosity was calculated by means of beam current monitor devices. Then, the cross section $\frac{d\sigma^3}{d\Omega_{e'} d\Omega_K dE_{e'}}$ was computed according to:

$$\frac{d\sigma^3}{d\Omega_{e'} d\Omega_K dE_{e'}} = \frac{N}{K_{sur} \cdot eff \cdot L \cdot PS \cdot LT}\,, \qquad (3)$$

where N is the event number in the experiment, eff is the global detector efficiency, LT is the detector live time, PS is the detector phase space, K_{sur} is the kaon survival in the HRS, L is the integrated luminosity, $\mathrm{d}\Omega_{e'}$ and $\mathrm{d}\Omega_K$ are the solid angular ranges of the detected scattered electrons and produced kaons respectively, and $\mathrm{dE}_{e'}$ is the energy range of the detected scattered electrons.

Fig. 3 shows the background-subtracted experimental binding-energy spectrum, together with Monte Carlo simulations[29] (red curve) and the same simulations with the radiative effects turned off (blue curve). The error bars in the data are statistical. The simulations used the five peak positions and widths listed as configuration α in Table IV. The red curve fits the experimental data well with a corresponding χ^2/ndf value of 36.69/35. Several other peak configurations, with different numbers, heights, positions and widths of the peaks, have been found to reproduce the red curve. All of those are also expected to generate the same spectrum (the blue curve of Fig. 3) when radiative corrections are turned off, since radiative corrections are independent of the assumptions regarding the number and type of the peaks that build up the experimental spectrum. In practice, the simulated data do not overlap perfectly with the experimental data, which produces small systematic errors on the radiatively corrected spectrum.

The unfolding for radiative corrections has been done bin-by-bin. The content of each bin of the radiatively corrected spectrum was obtained by multiplying the corresponding bin of the experimental spectrum by the ratio of the blue and red curves of Fig. 3 for that bin. In order to avoid possible removals of background enhancements or to artificially null the spectrum in the regions where the blue curve is zero, the ratio between the blue and red curves of Fig. 3 was performed after summing the background to each of them. The background value was then subtracted from the result of the product of the ratio with the corresponding bin. The result is shown in Fig. 4 which presents the radiatively unfolded experimental data (points with statistical errors) compared to a theoretical prediction (thin green line). The band at the bottom of the histogram represents the systematic errors in the radiative unfolding. The theoretical histogram was obtained using the procedure described in section II assuming an energy resolution of 730 keV (FWHM). Once radiative corrections have been applied,

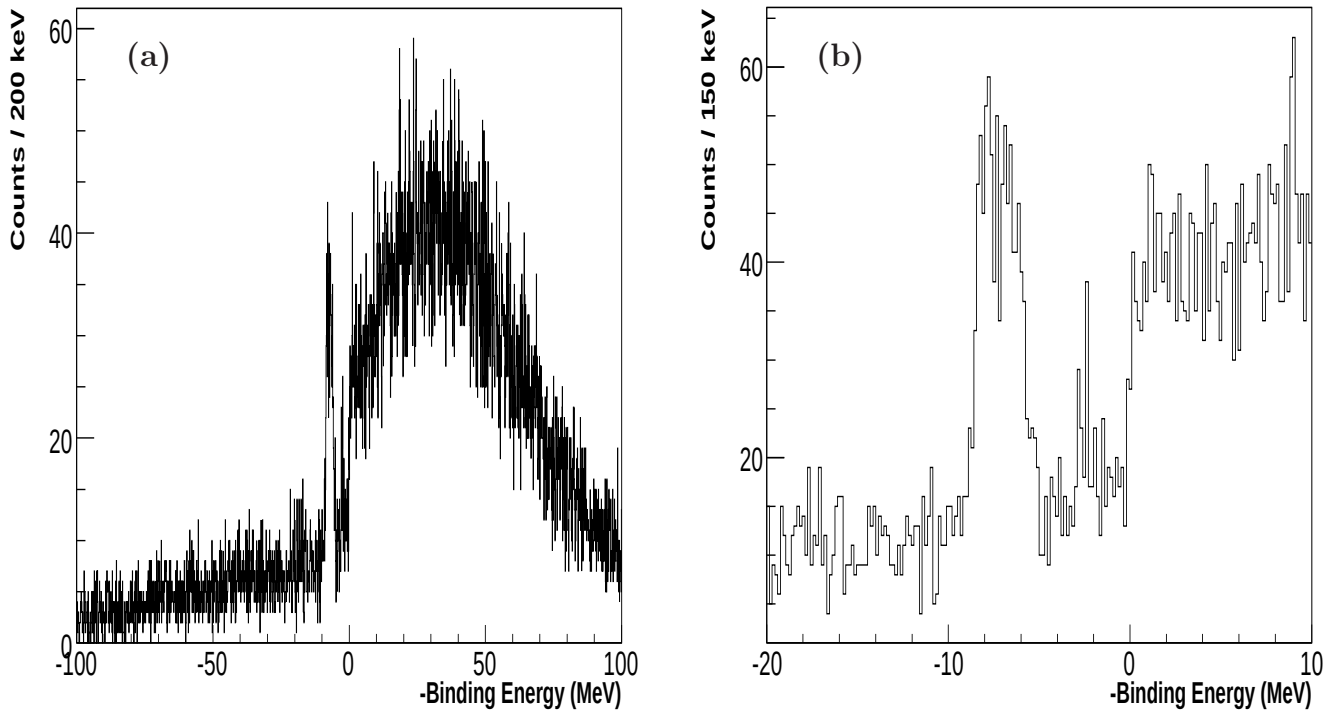

FIG. 2. The binding-energy spectrum obtained after kaon selection with aerogel detectors and RICH in (a) the whole energy range and (b) restricted to the region of interest.

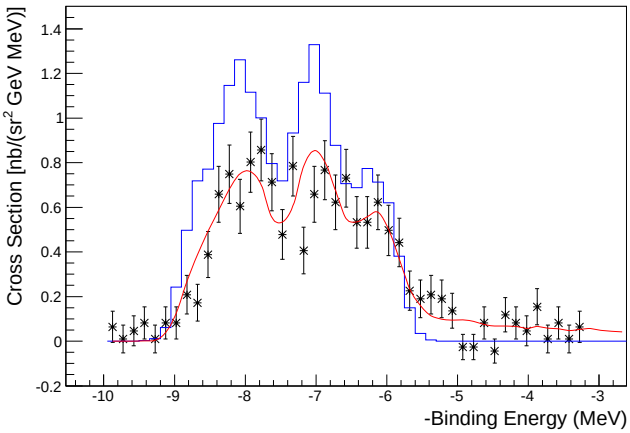

FIG. 3. (Color online) The $^{9}_{\Lambda}$Li differential cross section as a function of the binding energy. Experimental points vs. Monte Carlo results (red curve) and vs. Monte Carlo results with radiative effects turned off (blue histogram).

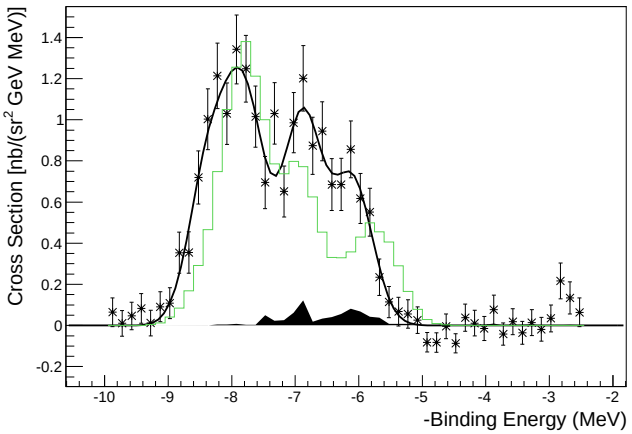

FIG. 4. (Color online) The radiatively unfolded experimental spectrum compared to a theoretical prediction (thin green line). The solid black line represents a fit to the data with four Gaussians of a common width. The theoretical curve was calculated with the width extracted from the fit (FWHM = 730 keV).

the binding-energy spectrum resolution is small enough to clearly show a three-peak structure in the spectrum. A more detailed description of the procedure employed to determine the radiatively unfolded spectrum of Fig. 4 is given in Appendix A.

IV. RESULTS

When analyzing the experimental spectrum in Fig. 4 one has to consider that, as explained in section II, the spectrum is made up by doublets and hence that each of the three peaks that appears in it is actually produced by the convolution of two "elementary" peaks. Because the

TABLE III. Excitation energies, widths, and cross sections obtained by fitting the ^{9}Be$(e,e'K^{+})^{9}_{\Lambda}$Li spectrum (first three columns), compared with theoretical predictions (last four columns). The last column gives the summed cross sections for the three doublets, to be compared with the experimental results in the third column.

Experimental data			Theoretical predictions			
E_x (MeV)	Width (FWHM) (MeV)	Cross section (nb/(sr^2 GeV))	E_x (MeV)	J^{π}	Cross section (nb/(sr^2 GeV))	Cross section Sum
0.00 ± 0.08	0.73 ± 0.06	0.59 ± 0.15	0.00	$3/2^{+}$	0.18	1.22
0.57 ± 0.12	0.73 ± 0.06	0.83 ± 0.13	0.59	$5/2^{+}$	1.04	
1.47 ± 0.09	0.73 ± 0.06	0.79 ± 0.07	1.43	$3/2^{+}$	0.29	0.59
			1.45	$1/2^{+}$	0.30	
2.27 ± 0.09	0.73 ± 0.06	0.54 ± 0.06	2.27	$5/2^{+}$	0.17	0.48
			2.74	$7/2^{+}$	0.31	

peaks of the spectrum are radiatively corrected, we assumed that all the elementary peaks were well described by Gaussian distributions. Considering the energy resolution to be constant over the whole spectrum range, we assumed in addition that the standard deviations of these Gaussians were equal. Although six Gaussian elementary peaks are expected, the possible existence of nearly degenerate doublets, or of doublets where one peak overwhelmingly dominates on the other, could reduce the number of elementary Gaussian peaks needed for the fit procedure following the Occam razor principle. The experimental spectrum in Fig. 4 was fitted in order to determine the positions, the heights, and the common standard deviation of the elementary peaks. The best fit was obtained with four Gaussian elementary peaks with a χ^2/n.d.f. value of 41.82/41. The energy resolution extracted from the fit, 730 keV (FWHM), is consistent with the value obtained in our previous analysis [30] and is in agreement with the measurements on $^{12}_{\Lambda}$B [4] and $^{16}_{\Lambda}$N [5]. The excitation energies (E_x) and cross sections extracted from the four-peak fit are reported in Table III where they are compared with the results calculated using the procedure described in section II for the six lowest states shown in Fig. 1. A fit with five Gaussian peaks produced the same result as shown in Table III with a χ^2/ndf value of 41.82/39 and a common FWHM for the peaks of 730 keV. The first three peaks had the same heights and positions of the corresponding peaks in Table III while the fourth and fifth peaks had equal positions, coincident with the binding energy of the fourth peak in Table III and heights whose sum was equal to the cross section value of the fourth peak in Table III. The result of the five-peak fit showed hence that only the ground-state doublet splitting could be detectable with the energy resolution of the experiment. A fit with three peaks also produced a result consistent with Table III, with a χ^2/ndf value of 47.52/43 and a common peak resolution extracted from the fit of 970 keV (FWHM). The first peak strength and position were equal (within one standard deviation) to the sum of the strengths and to the baricenter of the positions in the binding-energy spectrum of the first two states of Table III respectively. The other two peaks had strengths and positions equal (within one standard deviation) to the third and fourth peaks in Table III respectively. Fig. 4 and Table III show that the observed peak positions agree quite well with the predictions of the standard model for p-shell hypernuclei. The first multiplet can be decomposed into two peaks with a separation of 570 ± 120 keV that corresponds very well with the theoretical value of 590 keV. On the other hand, there is a systematic disagreement for the multiplet cross sections. In the first multiplet the 0.59 MeV ($5/2^{+}$) peak does not dominate as theoretically predicted (see Table III). The second and third multiplets are each observed as a single peak. This is probably due to the very close excitation energies of their two constituents (see Table III), although for the third multiplet it might be due to the fact that the strength of the 2.27 MeV ($5/2^{+}$) peak dominates over that of the other state.

In terms of the cross section, the spin-spin interaction (Δ) tends to deplete the spin-flip strength to the ground-state doublet and increase the non-spin-flip strength (see Fig. 1). The full reaction calculations include a number of spin-flip and non-spin-flip amplitudes, making the cross sections sensitive to the choice of the elementary reaction model. The SLA model was selected from the various isobar models because it gives the best results for the cross section. Spin-flip amplitudes are dominant in the SLA model which favors states in Fig. 1 with large $\Delta S = 1$ structure amplitudes. It is then clear that a model with larger non-spin-flip amplitudes might increase the relative cross sections for the $3/2^{+}_{1}$ and $5/2^{+}_{2}$ states and provide better agreement with the results of the experimental analysis. The cross section depends very much on the proton removal spectroscopic factors for ^{9}Be but, as is evident from Table II, theory agrees very well with the relative C^2S values derived from the analysis of two (d,^{3}He) studies, a reaction that has proven to be very reliable for such a comparison.

From the binding-energy spectrum of Fig. 4, a Λ sepa-

ration energy B_Λ of 8.36 ± 0.08 (stat.) ± 0.08 (syst.) MeV was obtained. This value agrees very well with the value 8.50 ± 0.12 MeV from emulsion data [31]. To determine this value the missing-mass scale needed to be calibrated because of uncertainties in the kinematical variables such as the primary electron energy and the central momenta and the central scattering angles of the scattered electrons and the produced kaons. For this calibration we took advantage of the fact that the experiment was performed just after the determination of the $^{12}_{\Lambda}$B excitation spectrum [4] that used the same experimental settings. Thus, the kinematical variables of the present experiment were determined, reproducing the binding energy of the $^{12}_{\Lambda}$B ground state at 11.37 ± 0.06 MeV [31]. A more detailed description of this missing-mass scale calibration is given in Appendix B.

V. SUMMARY

A high-quality $^{9}_{\Lambda}$Li hypernuclear spectrum has been obtained for the first time with sub-MeV energy resolution. The measured cross sections and the excitation energies of the doublets are in a good agreement with the values predicted using the SLA model and simple shell-model wave functions while a disagreement could exist with respect to the relative strengths of the states making up the first multiplet. As noted in the Sec. IV, an elementary model for the $(e, e'K^+)$ reaction with a different balance of spin-flip and non-spin-flip amplitudes might help to resolve this disagreement. A Λ separation energy B_Λ of 8.36 ± 0.08 (stat.) ± 0.08 (syst.) MeV was obtained, in good agreement with the emulsion value.

Appendix A: Radiative corrections

The procedure of unfolding radiative effects from an experimental spectrum does not depend on the choice of the peak structure used to fit the spectrum itself, providing that the fit describes the data reasonably. This property is very useful when the peak structure underlying an experimental spectrum is unknown as in Fig. 3, where several peak structures fit the experimental spectrum quite well and it is not obvious which of these structures is "the right one". To demonstrate the independence of radiative corrections from the energy spectrum structure, we define $Exp(E)$ as the function that describes the experimental spectrum. $Exp(E) \cdot dE$ is proportional to the number of events whose corresponding energy is in the interval $E \pm dE$. We define $S(E')$ as the function that describes the experimental spectrum in the absence of radiative effects. Lastly, we define $R(E' - E)$ as the probability that an event whose corresponding energy in the absence of radiative effects would have been E' has, because of the radiative effects, an energy equal to E. $Exp(E)$, $S(E')$ and $R(E - E')$ are related by

$$Exp(E) \cdot dE = dE \cdot \int dE' \cdot R(E' - E) \cdot S(E') \quad \text{(A1)}$$

For the sake of simplicity, we suppose in the following that $S(E')$ is equal to a sum of Gaussian peaks

$$S(E') = \sum_{k=1}^{N} A_k \cdot e^{-\frac{(E'-E_k)^2}{2\cdot\sigma_k^2}} , \quad \text{(A2)}$$

where A_k, E_k and σ_k are the amplitude, central value and standard deviation of the kth peak, respectively.

Let us assume two different peak configurations α and β, with N and M peaks, respectively, that produce two functions $S^\alpha(E')$ and $S^\beta(E')$ that are equal within the statistical error

$$S^\alpha(E') = \sum_{k=1}^{N} A_k e^{-\frac{(E'-E_k)^2}{2\cdot\sigma_k^2}} \approx \sum_{l=1}^{M} A_l e^{-\frac{(E'-E_l)^2}{2\cdot\sigma_l^2}} = S^\beta(E') \quad \text{(A3)}$$

This implies that for every value of E', $S^\alpha(E')$ and $S^\beta(E')$ have statistically compatible values and the χ^2 test

$$\chi^2 = \sum_j \frac{(S_j^\alpha - S_j^\beta)^2}{S_j^\alpha} , \quad \text{(A4)}$$

with

$$S_j^{\alpha,\beta} = \int_{E'_{j-1}}^{E'_j} dE' \cdot S^{\alpha,\beta}(E') , \quad \text{(A5)}$$

is acceptable within our confidence level. In Eq. (A5), $[E_{j-1}; Ej]$ is the jth interval that the energy spectrum is divided into.

It is obvious from Eq. (A1) that if $S^\alpha(E') = S^\beta(E')$ the two peak configurations α and β will produce the same experimental spectrum, that is $Exp^\alpha(E) = Exp^\beta(E)$.

The reverse is also true: if two peak configurations α and β produce two statistically compatible spectra ($Exp^\alpha(E) = Exp^\beta(E)$) then $S^\alpha(E') = S^\beta(E')$. In fact, defining

$$Exp_i = \int_{E_{i-1}}^{E_i} dE \cdot Exp(E) , \quad \text{(A6)}$$

and

$$R_{ij} = \int_{E_{i-1}}^{E_i} dE \cdot R(E' - E) , (E' \in [E'_{j-1}; E'_j]) \quad \text{(A7)}$$

we have from Eq. (A1)

$$\int_{E_{i-1}}^{E_i} dE \cdot Exp(E) = \int dE' \cdot S(E') \int_{E_{i-1}}^{E_i} dE \cdot R(E' - E) \quad \text{(A8)}$$

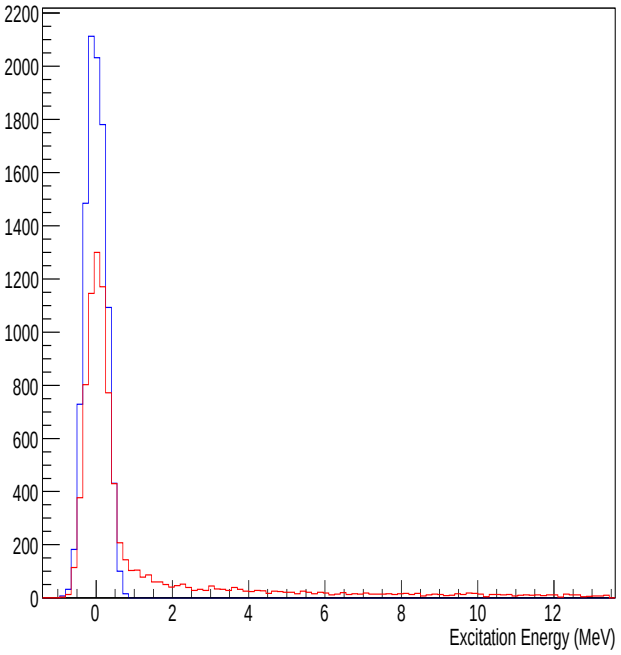

FIG. 5. (Color online) One peak of the excitation energy spectrum of the hypernucleus ${}^{9}_{\Lambda}$Li obtained through the reaction ^{9}Be$(e,e'K^{+})^{9}_{\Lambda}$Li as predicted by the Monte Carlo SIMC when including all effects (red curve) and "turning off" the radiative effects (blue curve). Arbitrary units. The position of the peak has been made coincident with the ground state.

Eq. (A8) means that

$$Exp_i = \sum_j R_{ij} \cdot S_j \tag{A9}$$

or, defining the arrays $\overrightarrow{Exp} \equiv \{Exp_1, Exp_2, ...Exp_i, ...\}$ and $\overrightarrow{S} \equiv \{S_1, S_2, ...S_j, ...\}$, and the matrix $R \equiv \{R_{11}, R_{12}, ..., R_{ij}, ...\}$

$$\overrightarrow{Exp} = R \cdot \overrightarrow{S} \tag{A10}$$

Defining at last R^{-1} as the inverse of the matrix R, we have

$$\overrightarrow{S} = R^{-1} \cdot \overrightarrow{Exp} \tag{A11}$$

From Eq. (A11) it follows that if $Exp^{\alpha}(E) = Exp^{\beta}(E)$ then $S^{\alpha}(E') = S^{\beta}(E')$. In fact,

$$\begin{aligned} Exp^{\alpha} = Exp^{\beta} \Rightarrow 0 &= R^{-1} \cdot (\overrightarrow{Exp^{\alpha}} - \overrightarrow{Exp^{\beta}}) \\ &= \overrightarrow{S^{\alpha}} - \overrightarrow{S^{\beta}} \Rightarrow S^{\alpha} = S^{\beta} \end{aligned} \tag{A12}$$

means that the spectrum with the radiative effects subtracted ($S(E')$) does not depend on the peak configurations α, β, $\cdots$ as long as all the configurations considered Exp^{α}, Exp^{β}, $\cdots$ fit the experimental spectrum with no radiative effects applied. It has to be noted that only two assumptions were made in deriving the conclusion quoted above

- the single intervals $[E_{j-1}; E_j]$ are so small that R_{ij} defined by Eq. (A7) is constant in it.

- The matrix R is invertible. This is usually the case considering that usually $R_{ii} \neq 0$ and $R_{ji} = 0$ if $R_{ij} \neq 0$ and $i \neq j$

TABLE IV. Columns 2 and 3: peak positions and relative amplitudes of five configurations α, β, γ, δ and ϵ for which the Monte Carlo SIMC predicts a ${}^{9}_{\Lambda}$Li excitation energy spectrum that fits the experimental data. Column 4: the χ^2 test values calculated through Eq. (A13) for these configurations.

Configuration	Peak Positions MeV	Peak Amplitudes Arbitrary units	χ^2 35 ndf
	0.00	2.23	
	0.64	3.54	
α	1.32	1.90	36.685
	1.71	2.61	
	2.35	2.33	
	0.00	2.08	
	0.58	3.48	
β	1.54	3.38	38.247
	2.37	2.10	
	0.00	2.34	
	0.54	3.88	
γ	1.49	3.78	46.088
	2.36	3.28	
	0.00	1.86	
	0.54	3.08	
δ	1.49	3.00	39.068
	2.36	2.06	
	0.00	1.85	
	0.65	3.09	
ϵ	1.43	3.00	39.000
	2.39	2.06	

To determine the spectrum with the radiative effects "turned off" (blue curve of Fig. 3) the Monte Carlo SIMC was employed [29]. The red curve of Fig. 5 shows a single peak of the ${}^{9}_{\Lambda}$Li excitation energy spectrum as predicted by SIMC for the reaction ^{9}Be$(e,e'K^{+})^{9}_{\Lambda}$Li when using the E94-107 experimental apparatus (position and amplitude of the peak are arbitrary). The blue curve of Fig. 5 shows the same peak when the radiative effects in the Monte Carlo SIMC are "turned off". Several peak configurations, made up by a number of peaks like the one of Fig. 5 red curve, fit the experimental ${}^{9}_{\Lambda}$Li excitation energy spectrum after being normalized to it. Table IV quotes five of them. Their corresponding excitation energy spectra (normalized to the experimental data) are shown in Fig 6. For each configuration, Table IV quotes the position and relative amplitude of the peaks (here and in the following the amplitude of a peak is defined as the integral of the peak over the whole energy spectrum)

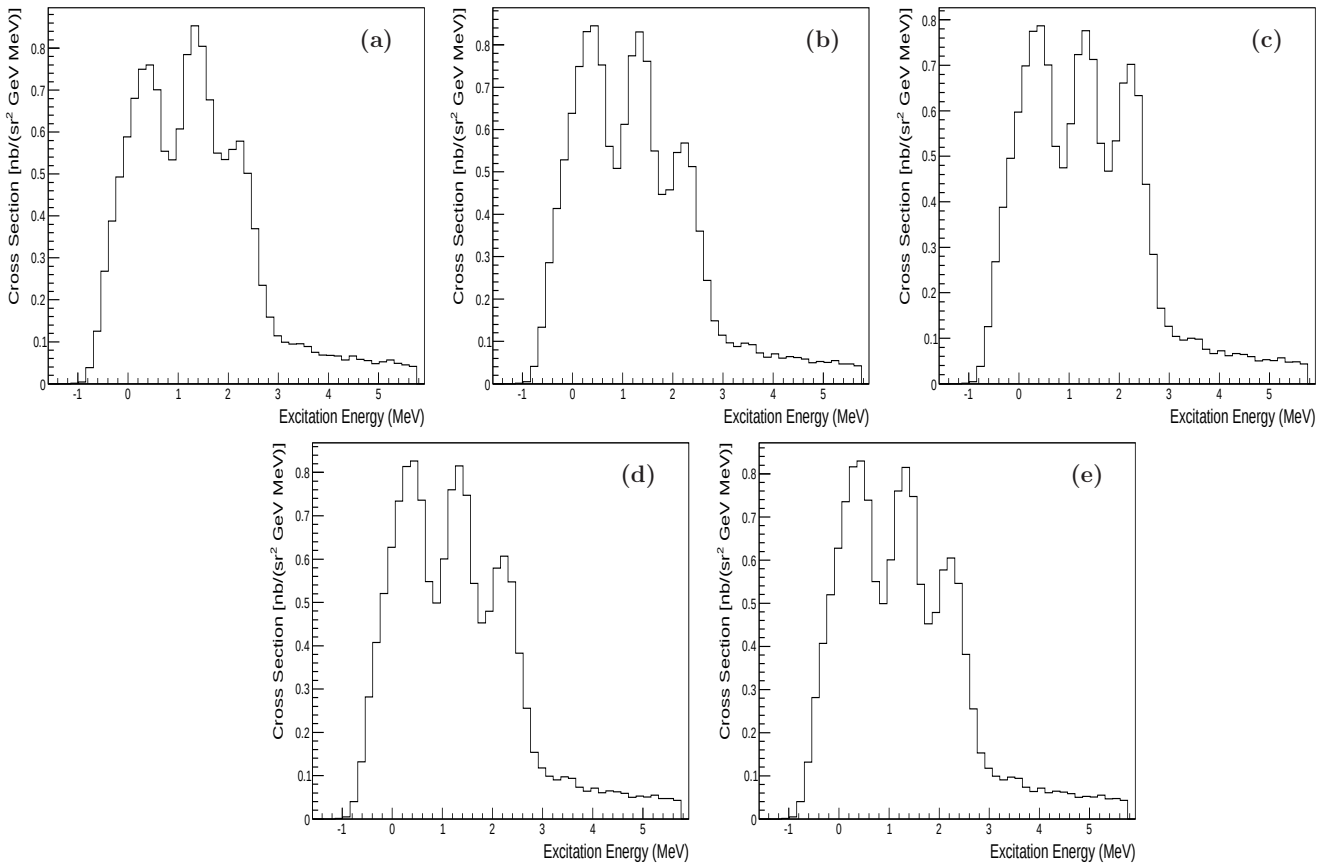

FIG. 6. $^{9}_{\Lambda}$Li excitation energy spectra as predicted by the Monte Carlo SIMC for the peak configurations α, β, γ, δ and ϵ quoted in Table IV (Panels (a), (b), (c), (d) and (e), respectively).

and the value of the χ^2 test,

$$\chi^2 = \sum_i \frac{(C_i^{conf} - Exp_i)^2}{Exp_i} \,, \qquad \text{(A13)}$$

where $conf = \alpha$, β, γ, δ, or ϵ, Exp_i is the number of counts in the ith interval of the experimental excitation energy spectrum, and C_i^{conf} is the number of counts in the same interval as predicted by the normalized peak configuration $conf$. The χ^2 tests were performed in the interval -1.515 MeV $<$ Excitation Energy $<$ 3.735 MeV, corresponding to 35 degrees of freedom.

Because of the properties of the subtraction of radiative effects from spectra quoted above, all the peak configurations α, β, γ, δ, and ϵ produce the same "radiatively corrected" spectrum. The spectra of Fig. 7 are obtained from Fig. 6 by turning off the radiative effects, that is replacing the "Fig. 5 red curve-like" peaks with "Fig. 5 blue curve-like" peaks, without changing positions and amplitudes of the peaks. All plots of Fig. 7 are quite equal, as confirmed by the χ^2 test,

$$\chi^2 = \sum_i \frac{(C_i^{conf_1} - C_i^{conf_2})^2}{C_i^{conf_1}} \,, \qquad \text{(A14)}$$

with $conf_1$ and $conf_2 = \alpha$, β, γ, δ, or ϵ. In the worst case ($conf_1 = \alpha$ and $conf_2 = \gamma$) Eq. (A14) yielded a value of 28.387 with 40 degrees of freedom.

In Fig. 8(a), Fig. 7(a) (dashed line) and Fig. 7(c) (continuous line) are shown together. Because the configurations α and γ produce the two most different "radiatively corrected" SIMC results, the difference between the two curves plotted in Fig. 8(a) was chosen as the systematic error due to the ambiguity of the peak structure underlying the energy spectrum. As shown in Fig. 8(b) this error is small compared to the statistical error.

The method to obtain radiative corrected spectra described in this Appendix was used, in the analysis of the $^{9}_{\Lambda}$Li spectrum, because of the difficulties in establishing the peak structure underlying the experimental spectrum. Its reliability is based on Eq. (A11), that is mathematically correct, and on the fact that the uncertainties on the radiative corrected spectrum $\overrightarrow{S}$ derived by Eq. (A11) are small because they originate from the very small uncertainties on the experimental spectrum $\overrightarrow{Exp}$ and on the function R^{-1} ("detector function" in the following). The uncertainties on the experimental spectrum $\overrightarrow{Exp}$ in the E94-107 experiment are very small, because

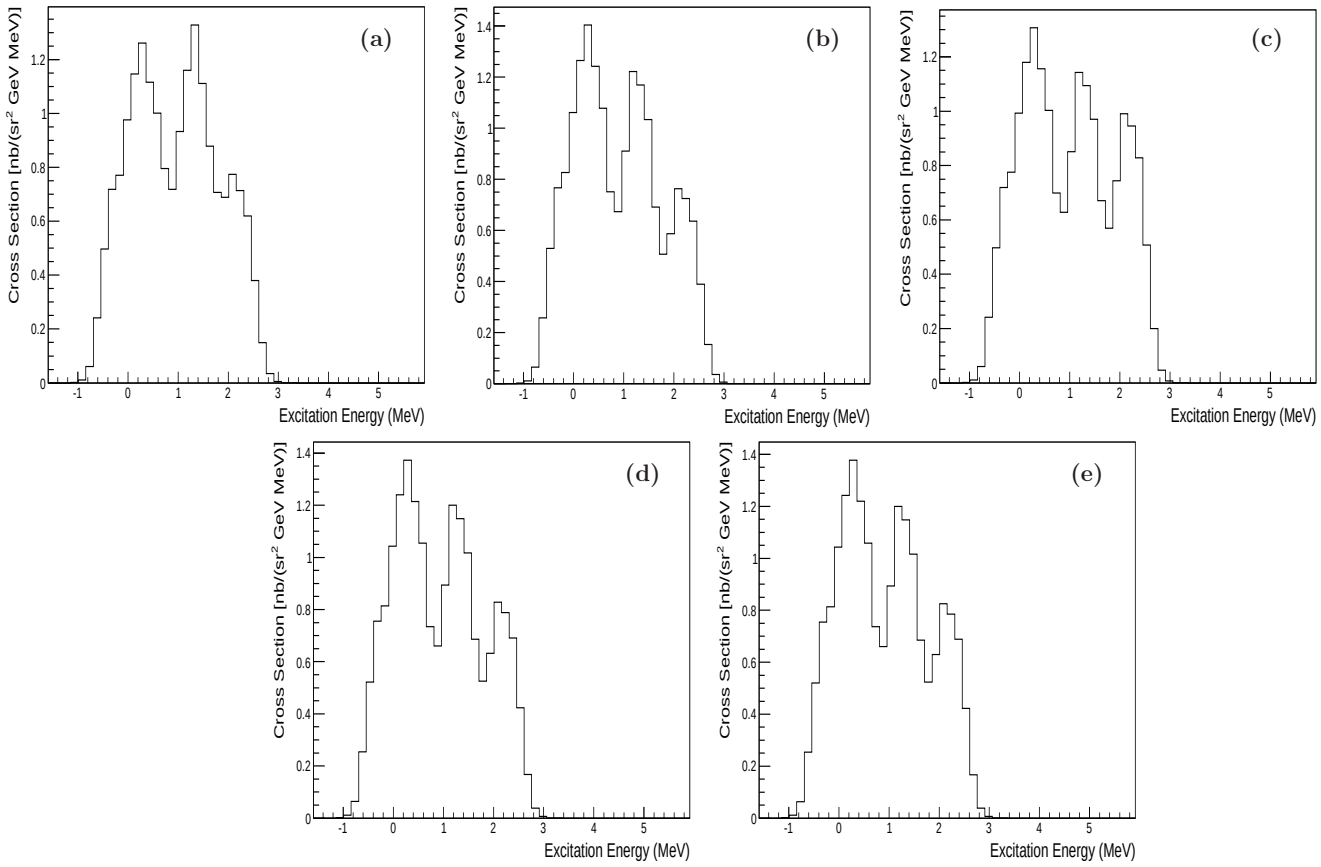

FIG. 7. $^{9}_{\Lambda}$Li excitation energy spectra as predicted by the Monte Carlo SIMC for the peak configurations α, β, γ, δ and ϵ quoted in Table IV, when the radiative effects are "turned off" (Panels (a), (b), (c), (d) and (e), respectively).

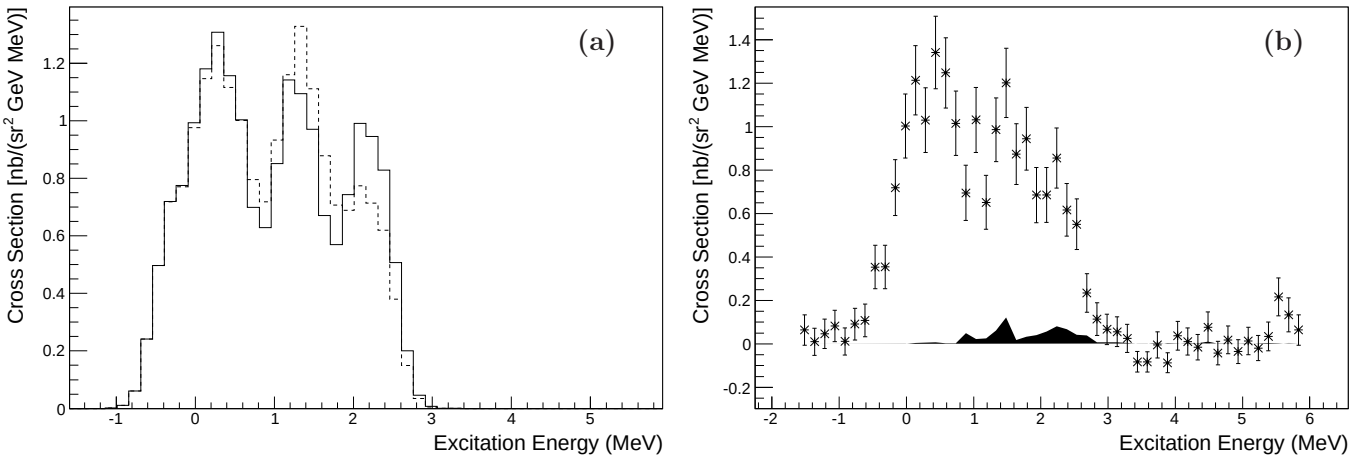

FIG. 8. (a) the spectrum of the configuration α (dashed line) and of the configutration γ (continuous line) as predicted by the Monte Carlo SIMC when the radiative effects are "turned off". (b) the statistical errors (error bars) and the systematic errors (full band) as a function of the excitation energy. The systematic error was defined as the difference between the dashed line and the continuous line of panel (a), see text for details.

the hypernuclei were generated in point-like targets and the experimental binding energy spectra were obtained by the measurements of the momenta and the scattering coordinates of the secondary electrons and of the produced kaons in the reaction $Z(e,e'K^+)Z-1$. These momenta and scattering coordinates were determined very precisely by magnetic spectrometers (at the level of 10^{-4} for the momenta measured by HRS arms). Besides, the energy losses of the secondary electrons and of the produced kaons inside the target and along the path to the detectors were small. Moreover, thanks to the excellent Particle Identification apparatus employed, the experimental spectrum of the experiment E94-107 was pratically background free, the only small background coming from kaons from accidental coincidences. The uncertainties on the detector function R^{-1} in Eq. (A11) are very small too because of the simple geometries involved, the small uncertainties on the scattering angles of the detected particles and of the very well known QED cross sections involved. All these considerations make the method to obtain radiative corrected spectra described in this Appendix even much more reliable of the formally similar and widely used method of determing neutron spectra from the proton recoil energy measurement (see for example [32, 33]), that is affected by sometimes not negligible uncertanties on the measured recoil proton energy (and consequently on the experimental spectrum) and on the detector function that depends on the geometry (and on the connected problem of the determination of the scattering angle of the detected proton) and on the degree of knowledge of the differential n - p scattering cross section.

Appendix B: Missing-mass scale

In the Hall A experimental setup, scattered electrons and produced kaons of the reactions $^9\mathrm{Be}(e,e'K^+)^9_\Lambda\mathrm{Li}$ and $^{12}\mathrm{C}(e,e'K^+)^{12}_\Lambda\mathrm{B}$ were detected by the High Resolution Spectrometer (HRS) electron arm and by the HRS hadron arm, respectively, while the primary electrons were provided by the CEBAF accelerator. The CEBAF accelerator electron beam energy and the central momenta and angles of the HRS electron and hadron arms were set according to the kinematics of the reactions and are taken as constant for the course of the experiment (their variations being of the order of 10^{-5} for the CEBAF electron beam energy and the central momenta of the HRS electron and hadron arms, and practically zero for the spectrometer central angles). However, the actual values of the CEBAF accelerator electron beam energy and of the central momenta and angles of the HRS electron and hadron arms, although constant, differ by unknown amounts from the nominal set values, and are referred to as "kinematical uncertainties". Although small (the experimental uncertainties on the CEBAF accelerator electron beam energy and on the spectrometer central momenta being of the order of 10^{-4} - 10^{-3} and those on the spectrometer central angles of the order of 10^{-2}), these kinematical uncertainties cause a global shift in the binding-energy spectrum that hence has to be calibrated. In fact, the binding energy is expressed as

$$E_{bind} = -\sqrt{(E_m)^2 - (P_m)^2} + M_{residue} + M_\Lambda \ , \quad \text{(B1)}$$

with

$$E_m = M_{Target} + E_e - E_{e'} - E_K \ , \quad \text{(B2)}$$

and

$$\vec{P}_m = \vec{P}_e - \vec{P}_{e'} - \vec{P}_K \ , \quad \text{(B3)}$$

where E_e, $\vec{P}_e$, $E_{e'}$, $\vec{P}_{e'}$, E_K, and $\vec{P}_K$ are the energies and the momenta of the primary electron, of the scattered electron and of the produced kaon respectively, M_Λ is the Λ mass, M_{Target} is the target mass, and $M_{residue}$ is the mass of the residual nucleus, that is of the nucleus with A-1 nucleons and Z-1 protons (where A is the number of nucleons and Z is the atomic number of the target, respectively).

The change in the binding-energy spectrum ΔE_{bind} caused by the kinematical uncertainties can be expressed by the formula

$$\begin{aligned}\Delta E_{bind} = {} & \frac{\partial E_{bind}}{\partial E_e}\cdot\Delta E_e + \frac{\partial E_{bind}}{\partial P_{E\_Arm}}\cdot\Delta P_{E\_Arm} \\ & + \frac{\partial E_{bind}}{\partial P_{H\_Arm}}\cdot\Delta P_{H\_Arm} + \frac{\partial E_{bind}}{\partial \phi_{E\_Arm}}\cdot\Delta\phi_{E\_Arm} \\ & + \frac{\partial E_{bind}}{\partial \phi_{H\_Arm}}\cdot\Delta\phi_{H\_Arm} \ , \end{aligned} \quad \text{(B4)}$$

where E_e is the CEBAF electron beam energy, P_{E_Arm} and P_{H_Arm} are the central momenta of HRS electron arm and HRS hadron arm, ϕ_{E_Arm} and ϕ_{H_Arm} are the central angles (defined as the angles between the central axes and the CEBAF beam line) of HRS electron arm and HRS hadron arm, and ΔE_e, ΔP_{E_Arm}, ΔP_{H_Arm}, $\Delta\phi_{E\_Arm}$ and $\Delta\phi_{H\_Arm}$ are the kinematical uncertainties, that is the differences between the nominal and the actual values of the CEBAF electron beam energy and of the central momenta and the central angles of HRS electron and HRS hadron arms. $\vec{P}_e$, $E_{e'}$, $\vec{P}_{e'}$, E_K, and $\vec{P}_K$ in Eq. (B1) - (B3) are functions of E_e, P_{E_Arm}, P_{H_Arm}, ϕ_{E_Arm} and ϕ_{H_Arm}, as well as (with the exception of $\vec{P}_e$) of the scattering variables. For example, the components normal to the beam line in the horizontal plane of $\vec{P}_{e'}$ and $\vec{P}_K$ respectively (called here $P_{e'_x}$ and P_{K_x}, respectively) are given by the expressions $P_{e'_x} = P_{E\_Arm}\cdot(1+\delta_{e'})\cdot\cos(\theta_{e'})\cdot\sin(\phi_{E\_Arm}+\phi_{e'})$ and $P_{K_x} = P_{H\_Arm}\cdot(1+\delta_K)\cdot\cos(\theta_K)\cdot\sin(\phi_{H\_Arm}+\phi_K)$, while $E_{e'} = P_{E\_Arm}\cdot(1+\delta_{e'})$ and $E_K = \sqrt{(P_{H\_Arm}\cdot(1+\delta_K))^2 + m_k^2}$, where $\delta_{e'}$ (δ_K) is the percentage difference between the momentum of the scattered electron (produced kaon) and the central momentum of the HRS electron arm (HRS hadron arm), $\phi_{e'}$ (ϕ_K) is the angle between the electron (produced kaon) direction in the horizontal plane and ϕ_{E_Arm}

(ϕ_{H_Arm}), $\theta_{e'}$ (θ_K) are the angles between the electron (produced kaon) direction in the vertical plane and the CEBAF beam line, and m_K is the kaon mass.

Considering Eqs. (B1), (B2), and (B3), Eq. (B4) is equal to

$$\Delta E_{bind} = (-\Delta E_e + \Delta P_{E\_Arm} + \Delta P_{H\_Arm}) \times \frac{M_{Target} + E_e - E_{e'} - E_K}{\sqrt{(M_{Target} + E_e - E_{e'} - E_K)^2 - (\vec{P}_e - \vec{P}_{e'} - \vec{P}_K)^2}} + \frac{f}{2 \cdot \sqrt{(M_{Target} + E_e - E_{e'} - E_K)^2 - (\vec{P}_e - \vec{P}_{e'} - \vec{P}_K)^2}} \quad \text{(B5)}$$

where

$$f = \frac{\partial(\vec{P}_m)^2}{\partial E_e} \cdot \Delta E_e + \frac{\partial(\vec{P}_m)^2}{\partial P_{E\_Arm}} \cdot \Delta P_{E\_Arm} + \frac{\partial(\vec{P}_m)^2}{\partial P_{H\_Arm}} \cdot \Delta P_{H\_Arm} + \frac{\partial(\vec{P}_m)^2}{\partial \phi_{E\_Arm}} \cdot \Delta \phi_{E\_Arm} + \frac{\partial(\vec{P}_m)^2}{\partial \phi_{H\_Arm}} \cdot \Delta \phi_{H\_Arm} \quad \text{(B6)}$$

For the kinematics of the experiment E94-107 (see the nominal values of E_e, $E_{e'}$, and E_K at the end of this Appendix) or if $M_{\rm Target} \gg E_e, E_{e'}, E_K$, the change in the binding-energy spectrum ΔE_{bind} caused by the kinematical uncertainties is

$$\Delta E_{bind} \sim S + T\,, \quad \text{(B7)}$$

where

$$S = -\Delta E_e + \Delta P_{E\_Arm} + \Delta P_{H\_Arm}\,, \quad \text{(B8)}$$

and

$$T = M^{-1}_{\rm Target} \cdot \frac{f}{2}\ . \quad \text{(B9)}$$

The term S does not depend on the target mass and causes a global shift of the binding-energy spectrum without changing the peak shapes and relative positions, while the term T is equal to zero only when $0 = \Delta E_e = \Delta P_{E\_Arm} = \Delta P_{H\_Arm} = \Delta \phi_{E\_Arm} = \Delta \phi_{H\_Arm}$. When this condition is not fulfilled, the main effect of T on the binding-energy spectrum is to broaden the peaks because, in this case, depending on scattering variables through $\vec{P}_m$, it produces non-zero, scattering variable dependent values of ΔE_{bind} and, as a consequence, an unphysical dependence on the scattering variables of the binding energy that broadens the peaks corresponding to the bound states. Because of the presence of the coefficient $M^{-1}_{\rm Target}$, the effect of T on the position of the peaks is negligibly small.

The actual values of E_e, P_{E_Arm}, P_{H_Arm}, ϕ_{E_Arm}, and ϕ_{H_Arm} are hence those for which $S = T = 0$ (which places a peak at its known position in the binding energy spectrum and minimizes its FWHM).

To determine the Λ binding energy of the hypernucleus ${}^{9}_{\Lambda}$Li produced in the reaction ^{9}Be$(e,e'K^+){}^{9}_{\Lambda}$Li, we took advantage of the fact that the experiment used the same set-up employed for the study of the ${}^{12}_{\Lambda}$B hypernucleus. The values of E_e, P_{E_Arm}, P_{H_Arm}, ϕ_{E_Arm}, and ϕ_{H_Arm} were thus the same in the productions of both ${}^{9}_{\Lambda}$Li and ${}^{12}_{\Lambda}$B and were determined by positioning the ${}^{12}_{\Lambda}$B ground state at its known position of 11.37 ± 0.06 MeV [31] in the binding-energy spectrum and minimizing its FWHM. When minimizing the ${}^{12}_{\Lambda}$B ground-state FWHM, it has to be taken into account that this ground state is actually a doublet whose energy splitting, assumed to be equal to the ${}^{12}_{\Lambda}$C ground-state energy splitting, is 161.6 ± 0.2 keV [34, 35]. Minimizing the ${}^{12}_{\Lambda}$B ground-state FWHM implies hence some sort of distortion because it artificially narrows the positions of the peaks making up the doublet. However, the ${}^{12}_{\Lambda}$B ground-state doublet energy splitting is small enough with respect to the energy resolution of the experiment to make the approximation of assuming the ${}^{12}_{\Lambda}$B ground state as a single peak still valid. No attempt to minimize the FWHM was performed on the other peaks of the ${}^{12}_{\Lambda}$B binding-energy spectrum. Another possibile source of distortion comes from the term T in Eq. (B7), which, although small because of the presence of the factor M^{-1}_{Target} in it (see Eq. (B9)), can potentially change the positions of the excited states with respect to each other and with respect to the ground state. During all the process of minimization of the kinematical uncertainties, the positions of the peaks of the ${}^{12}_{\Lambda}$B energy spectrum as resulted by a fitting procedure were checked to ensure that the relative peak positions did not change within the errors (the error of a position peak being defined as the standard deviation resulting by the fitting procedure). It has to be stressed that the term S in the expression of ΔE_{bind} given by Eq. (B7) dominates because of the presence of the factor M^{-1}_{Target} in the term T (see Eq. (B9)). The positioning of the ${}^{12}_{\Lambda}$B ground state at its known value in the binding spectrum was thus mainly performed choosing a set of values ΔE_e, ΔP_{E_Arm}, and ΔP_{H_Arm} that produced a value of S equal to the difference between the measured and the expected position of the ${}^{12}_{\Lambda}$B ground state. The minimization of the ${}^{12}_{\Lambda}$B ground state peak FWHM produces only second order effects on the position of the peaks in the binding-energy spectrum and was peformed mainly to choose the right set of values ΔE_e, ΔP_{E_Arm}, and ΔP_{H_Arm} among the ∞^2 sets of values that produced the desired value of S. Things are much different for the reaction $p(e,e'K^+)\Lambda$, where the target mass is small and the minimization of the FWHM of the peak (which is a single peak) plays a role as important as the positioning of the peak in the binding-energy spectrum to its zero value.

The procedure described above resulted in the set of values $E_e = 3775.38$ MeV, $P_{E\_Arm} = 1573.63$ MeV, $P_{H\_Arm} = 1955.79$ MeV, $\phi_{E\_Arm} = -5.940°$, and $\phi_{H\_Arm} = 6.050°$. Replacing with these values the nominal ones $E_e = 3774.96$ MeV, $P_{E\_Arm} = 1570$ MeV,

$P_{H\_Arm} = 1960$ MeV, $\phi_{E\_Arm} = -5.873°$, and $\phi_{H\_Arm} = 6.131°$ in the E_{bind} expression, a value of 8.36 ± 0.08 (stat.) MeV was obtained for the ${}^{9}_{\Lambda}$Li ground state.

The statistical error of ± 0.08 MeV is the error in the position of the first peak in the four-Gaussian fit of the ${}^{9}_{\Lambda}$Li binding-energy spectrum (see Fig. 4 and Table III). When evaluating the systematic error of the ${}^{9}_{\Lambda}$Li binding energy, one has to consider that, as quoted above, the term S in ΔE_{bind} dominates the effects of the term T. When neglecting the energy loss in the target, this means that if the single values of ΔE_e, ΔP_{E_Arm}, and ΔP_{H_Arm} were wrong, the ${}^{9}_{\Lambda}$Li binding energy would not be affected significantly as long as the sum S (and hence the position of the ${}^{12}_{\Lambda}$B ground state) is correctly reproduced. The major source of systematic error is hence due to the energy loss in the target. The difference between the shifts of the ground-state position in the ${}^{12}_{\Lambda}$B and ${}^{9}_{\Lambda}$Li binding-energy spectra due to the energy loss in the targets of ^{12}C and ^{9}Be, respectively, was evaluated to be equal to 50 keV through the use of the Monte Carlo code SIMC [29]. This value was added in quadrature to the error of 60 keV quoted for the ${}^{12}_{\Lambda}$B ground-state binding energy [31] to give a 80 keV systematic error on the ${}^{9}_{\Lambda}$Li binding energy.

ACKNOWLEDGMENTS

We want to remember F. Cusanno, who enthusiastically and greatly contributed to this paper before his untimely death. We acknowledge the Jefferson Lab Physics and Accelerator Division staff for the outstanding efforts that made this work possible. This material is based upon work supported by the Department of Energy, Office of Energy Research, under contract DE-AC05-06OR23177, by the Italian Istituto Nazionale di Fisica Nucleare, by the Grant Agency of the Czech Republic under grant No. P203/12/2126, by the French CEA and CNRS/IN2P3, and by the U.S. National Science Foundation.

[1] O. Hashimoto and H. Tamura, Prog. Part. Nucl. Phys. **57**, 564 (2006).
[2] H. Tamura *et al.*, Nucl. Phys. A **804**, 73 (2008).
[3] T. Motoba, P. Bydzovsky, M. Sotona, and K. Itonaga, Prog. Theor. Phys. Suppl. **185**, 224 (2010).
[4] M. Iodice *et al.*, Phys. Rev. Lett. **99**, 052501 (2007).
[5] F. Cusanno *et al.*, Phys. Rev. Lett. **103** 202501 (2009).
[6] T. Miyoshi *et al.*, Phys. Rev. Lett. **90**, 232502 (2003);
[7] L. Yuan *et al.*, Phys. Rev. C **73**, 044607 (2006);
[8] S.N. Nakamura *et al.*, Phys. Rev. Lett. **110**, 012502 (2013).
[9] F. Garibaldi, S. Frullani, P. Markowitz and J. LeRose, spokespersons, JLab Experiment E94-107, High Resolution 1p shell Hypernuclear Spectroscopy (1994).
[10] M. Sotona and S. Frullani, Prog. Theor. Phys. Suppl. **117**, 151 (1994).
[11] D. J. Millener, Nucl. Phys. A **804**, 84 (2008).
[12] D. J. Millener, Nucl. Phys. A **881**, 298 (2012).
[13] T. Mizutani, C. Fayard, G.-H. Lamot and B. Saghai, Phys. Rev. C **58**, 75 (1998).
[14] D. J. Millener, in *Topics in Strangeness Nuclear Physics*, Lecture Notes in Physics, Vol. 724, edited by P. Bydžovský, A.Gal, and J. Mares (Springer, New York, 2007), p. 31.
[15] U. Schwinn, G. Mairle, G. J. Wagner and Ch. Rämer, Z. Phys. A **275**, 241 (1975).
[16] M. A. Oothoudt and G. T. Garvey, Nucl. Phys. A **284**, 41 (1977).
[17] S. Cohen and D. Kurath, Nucl. Phys. **73**, 1 (1965).
[18] G.-B. Liu and H. T. Fortune, Phys. Rev. C **38**, 1985 (1988).
[19] S. Cohen and D. Kurath, Nucl. Phys. A **101**, 1 (1967).
[20] J. Alcorn *et al.*, Nucl. Instrum. Methods Phys. Res., Sect. A **522**, 294 (2004).
[21] G. M. Urciuoli *et al.*, Nucl. Phys. A **691**, 43c (2001).
[22] M. Iodice *et al.*, Nucl. Instrum. Methods Phys. Res., Sect. A **553**, 231 (2005).
[23] F. Garibaldi *et al.*, Nucl. Instrum. Methods Phys. Res., Sect. A **502**, 117 (2003).
[24] F. Cusanno *et al.*, Nucl. Instrum. Methods Phys. Res., Sect. A **502**, 251 (2003).
[25] G. M. Urciuoli *et al.*, Nucl. Instrum. Methods Phys. Res., Sect. A **612**, 56 (2009).
[26] R. Perrino *et al.*, Nucl. Instrum. Methods Phys. Res., Sect. A **457**, 571 (2001).
[27] L. Lagamba *et al.*, Nucl. Instrum. Methods Phys. Res., Sect. A **471**, 325 (2001).
[28] S. Marrone *et al.*, Nuovo Cimento B **124**, 99 (2009).
[29] R. Ent *et al.*, Phys. Rev. C **64**, 054610 (2001); https://hallcweb.jlab.org/wiki/index.php/Monte_Carlo.
[30] F. Cusanno *et al.*, Nucl. Phys. A **835**, 129 (2010); F. Garibaldi *et al.*, Nucl. Phys. A **914**, 34 (2013).
[31] M. Jurić *et al.*, Nucl. Phys. B **52**, 1 (1973).
[32] M. Baba *et al.*, Nucl. Instrum. Methods Phys. Res., Sect. A **428**, 454 (1999).
[33] A. Donzella *et al.*, Nucl. Instrum. Methods Phys. Res., Sect. A **613** , 58 (2010).
[34] Y. Ma *et al.*, Nucl. Phys. A **835**, 422 (2010).
[35] K. Hosomi *et al.*, Nucl. Phys. A **914**, 184 (2013).